minerals

MDPI

Article

Cement Render and Mortar and Their Damages Due to Salt Crystallization in the Holy Trinity Church, Dominicans Monastery in Cracow, Poland

Mariola Marszałek *, Krzysztof Dudek and Adam Gaweł

Department of Mineralogy, Petrography and Geochemistry, AGH University of Science and Technology, al. Mickiewicza 30, 30-059 Kraków, Poland; kadudek@agh.edu.pl (K.D.); agawel@agh.edu.pl (A.G.)

* Correspondence: mmarszal@agh.edu.pl

Received: 22 June 2020; Accepted: 17 July 2020; Published: 20 July 2020

Abstract: The investigations focused on the façade of the 17th-century Myszkowskis chapel at the 13th-century Church of the Holy Trinity in Cracow, Poland. Most of the chapel's façade is made of rusticated limestone blocks, but its lower part is covered with cement render, and the basement consists of irregular pieces of limestone and sandstone, bound and partly replaced with cement mortar. The façade exhibited clearly visible damages: gray soiling of the surface, cracks, scaling, and efflorescence. The study presents characteristics of the cement render and mortar used for stone repair and/or substitution, as well as efflorescence from the lower part of the Myszkowskis chapel façade. The materials were analyzed with optical microscopy, scanning electron microscopy (SEM-EDS), Raman microspectroscopy, X-ray diffractometry (XRPD), and mercury intrusion porosimetry. The analyses demonstrated that the render covering some of the decayed limestone blocks was prepared using Portland cement (residual clinker grains represent alite and belite) as a binding agent, mixed with crushed stone as an aggregate. The cement mortar consisted of rounded quartz grains, rock fragments, and feldspars in very fine-grained masses of calcite and gypsum, also containing relics of cement clinker (alite, belite, ferrite, and aluminate). All these components point out the use of the ordinary Portland cement. Analyses of the efflorescence allowed us to distinguish several secondary salts, among others, thenardite, aphthitalite, and darapskite. The appearance of these phases is related to the composition and physicochemical properties of the building materials, atmospheric alteration agents, air pollution, and some other anthropogenic factors.

Keywords: cement render; cement mortar; Portland cement; deterioration; secondary salts

1. Introduction

Construction mortars consist of various inorganic or organic binding materials and natural or artificial aggregates with or without pigments. Inorganic binders may be lime, cement, silica gel, or gypsum, and organic ones can be animal glue, polyester, acrylic or epoxy resins, whereas aggregates are most often sand or gravel. The kind of binder depends on the application area, climatic conditions and, in particular, on the moisture transport and mechanical properties of stones. Inorganic or organic additives are often used to adapt the mortar properties to the stone and to improve its durability. Repair and joint mortars have been used to fill open masonry joints or to repair and replace smaller missing parts of dimension stones, ornaments, and sculptures since antiquity [1].

Natural cement, called Roman cement (RC), was invented at the end of the 18th century and played an important role until the 1860s, when the artificial Portland cements (PC) gained broader usage. RC is still in use in conservation because the restoration of historic masonry requires materials with physico-chemical and mechanical properties similar to the original ones [2–6].

Roman cements are produced by firing marls (limestone containing a significant amount of clay) between 800 and 1200 °C (i.e., below their sintering temperatures). Ordinary Portland cement is usually produced by firing a ground mixture of limestone and clay in a temperature range of 1440 to 1480 °C (vitrification) [4,7–9]. The natural mixture of lime and clay (source of silica, alumina, and iron oxide) in the marl allows for RC synthesis at low temperatures, which could not be attained in any man-made mixture [2,4]. The main characteristics of RC were a short setting time (of around 15 min), warm (yellow-to-brown) color, little shrinkage on setting and good durability to atmospheric conditions and salt crystallization [2,4]. This made Roman cement a favored material for the easy manufacture of ornaments and renders for the exterior of buildings in the 19th/early 20th century (European Historicism and Art Nouveau period) [4].

Different calcination temperatures of Roman and Portland cements cause differences in their phase compositions [4,9]. While belite—C_2S (dicalcium silicate, $2CaO{\cdot}SiO_2$)—is the major hydraulic phase in Roman cements, alite—C_3S (tricalcium silicate, $3CaO{\cdot}SiO_2$)—is the major phase in ordinary Portland cement. Next to belite (as a mixture of two structural modifications β and α′, with the latter being predominant), the following compounds eventually form in an RC: wollastonite (monocalcium silicate, $CaO{\cdot}SiO_2$, CS); gehlenite (dicalcium aluminosilicate, $2CaO{\cdot}Al_2O_3{\cdot}SiO_2$, C_2AS); aluminate (tricalcium aluminate, $3CaO{\cdot}Al_2O_3$, C_3A); ferrite, also called brownmillerite (tetracalcium aluminoferrite, $4CaO{\cdot}Al_2O_3{\cdot}Fe_2O_3$, C_4AF) [2,4,7,9]. The major compounds present in PC clinkers, next to alite (predominant component, making up 50–70%), are belite (which makes up 15–30%), aluminate (C_3A), and ferrite (C_4AF) [9]. In contrast to PC, alite cannot form in RC because of low calcination temperatures. After hydration, both belite (β- and α′-belite) and alite form hydrated calcium silicates (CSH phases), being the main components of the cements, next to portlandite $Ca(OH)_2$. Unreacted and unhydrated components of Roman cements (in good quality cements present only in very small quantities)—calcium silicates: β-belite (as less reactive then α′-belite), gehlenite (C_2AS), and wollastonite (CS)—can be labelled as Roman cement fingerprint phases [2,4], like relics of alite (C_3S), which are characteristic of ordinary PC and are absent in RC [5,9].

As most calcareous materials exposed in urban environment, RC and PC undergo atmospheric sulphation, resulting in their alteration. Soluble sulphates can react with the cement components to form various salts, such as ettringite $Ca_6Al_2(SO_4)_3(OH)_{12}{\cdot}26H_2O$ and gypsum $CaSO_4{\cdot}2H_2O$ [2,10–12]. Crystallization of secondary salts, being the most efficient deterioration process in porous materials, may substantially contribute to the damaging of building materials. The most important damaging factor is crystallization pressure during salt precipitation, resulting in the formation of cracks and loss of cohesion between the material components [13]. The crystallization can occur at the surface (efflorescence) or within the porous structure of the building materials, in confined spaces (subflorescence). Mineralogical and chemical changes in cement, due to water penetration through and dissolution of the material components, can lead to structural changes by favoring cracks and material disintegration. Rainwater infiltration, bringing about both the crystallization and dissolving of salts over an extended period of time, can contribute to the disintegration of building materials.

The investigations presented are focused on the southern wall façade of the 17th-century Myszkowskis Chapel, a part of the 13th-century Church of the Holy Trinity at the Dominicans monastery in Cracow, Poland. The chapel, founded by Zygmunt Myszkowski and his brother Alexander as the family mausoleum [14], was most likely designed by Santi Gucci from Florence (Italy) and built by masters from his workshop. The substantial part of the façade is covered with a Mannerist rustication [15,16] made of regular blocks of the Middle Miocene (Early Badenian), lithothamnium limestone, so-called Pińczów limestone, quarried in and near Pińczów (Carpathian Foredeep, South-Central Poland) [17,18]. Rusticated blocks are underlain by a small, horizontal element in the shape of a shaft, and a belt consisting of two rows of rectangular, plain limestone blocks, without rustication. The next lowest part of the façade wall, close to the pavement level, consists of rectangular bright blocks of various dimensions, as shown in Figure 1. Available sources [17–19] and unpublished conservatory documentations yielded some information about the rusticated Pińczów

limestone, but any detailed information about the other elevation materials was not encountered. In the course of our previous research [20], we observed that the stony elements below the rusticated blocks of the Pińczów limestone were also covered with a thin layer of a beige-brown, highly exfoliated cement render. However, some of the limestone blocks in the row of the façade below the small shaft contained replacements and thick, bright render of a different nature than the previous.

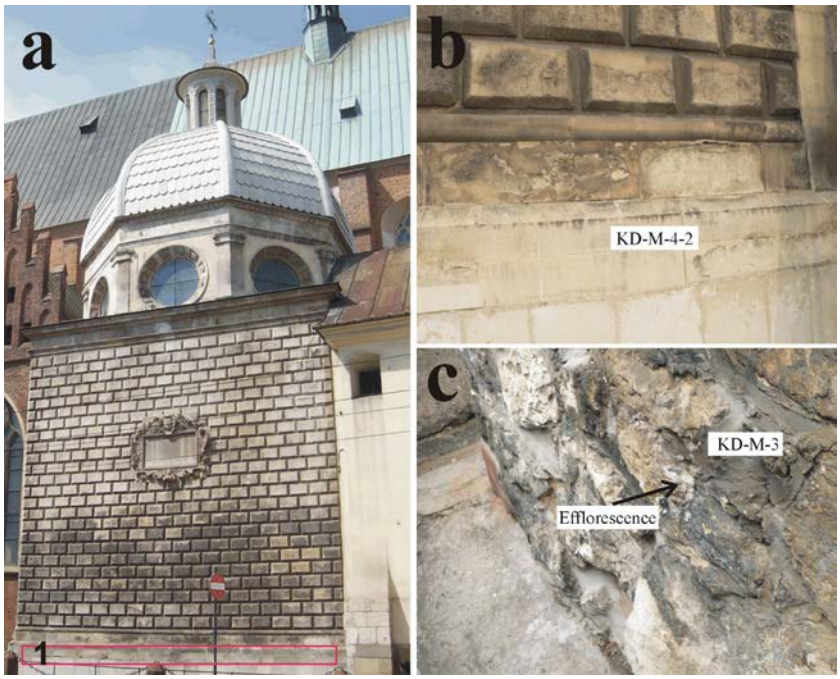

Figure 1. Myszkowskis Chapel of the Holy Trinity Church in Cracow (**a**) and sites of sampling: rusticated wall and elements beneath (**b**); exposed part of the foundations (**c**) (after [20], modified). The samples represent: KD-M-4-2—bright, cement rendered part of the elevation; KD-M-3—cement mortar from the subwall, in places covered with salt efflorescence. (1)—sampling area in detail in (b); area presented in (c) is located beneath the pavement level, below the area marked as (1). Photos (b) and (c) by K. Bałaga.

The exposed foundations of the chapel (subwall) are made of irregular pieces of bright limestones and gray sandstones, bound with and partly replaced by a cement mortar. The Upper Jurassic limestones most likely came from quarries in close vicinity, north or northwest from the Old Town of Cracow [21]. The sandstones proved to represent the Upper Cretaceous Istebna sandstones and were probably quarried a few tens of kilometers south of Cracow in the Flysch Carpathians. The mortar was applied unevenly; in some places covers the stony elements, and in others forms convex welds.

The façade exhibits clear signs of damage that include dark gray soiling of the surface, black crusts, surface exfoliations, cracks and fine-crystalline salt efflorescence. The last three are mainly associated with the elements covered with render, however, efflorescence occurs only on the lower part of the subwall, chiefly on the border between the limestone blocks and the cement mortar. The part of the façade with rectangular bright blocks does not reveal clear signs of damage.

No detailed information on conservation work on the chapel's façade was encountered; however, it can be suspected that many conservation interventions were carried out during its history. Nonetheless, it is known that following the damages brought about by the fire of 1850, the chapel was renovated under direction of Z. Hendel in the years 1900–1910 [22]. In 1959, a thorough conservation was carried out by the Historical Monuments Conservation Labs. Bright replacements of the material below the shaft could have been applied both by Hendel during the works of 1900–1910 (the drain ditch, unveiling the subwall, was probably made by Hendel) and by Historical Monuments Conservation Labs (R. Rolewicz, a stone conservator, personal communication).

The presented study began during conservatory works in 2017, thanks to the courtesy of the Monastery authorities and Mr Bartłomiej Polczyński. Some of the results were published in 2019 [20]. Current research was focused on a bright render, in places covering the limestone blocks and filling the material losses (lower part of the façade wall, just above the bright blocks, close to the pavement level) and mortar that bound and partly replaced the stones in the chapel subwall, below the pavement line. The study was also aimed at characteristics and the determination of the render and mortar cement(s), as well as signs of their deterioration.

2. Materials and Methods

Samples selected for the studies represent two types of the building materials taken from the Myszkowskis Chapel façade and subwall, as shown in Figure 1: a piece of the wall in places covered and/or filled with bright cement render, above the pavement level (samples labelled KD-M-4-2), and the cement mortar between stony blocks in the subwall below the pavement level (samples labelled KD-M-3). Salt efflorescences from the contacts between the limestone surface and the cement mortar, observed in the lower part of the subwall, were analyzed as well.

Laboratory tests included mineralogical, chemical, and petrophysical analyses. Optical microscopy, scanning electron microscopy (SEM-EDS), Raman microspectroscopy, and X-ray diffractometry (XRPD) were used for analyzing the materials and deterioration products of the cement render and mortar. The petrophysical properties of the materials were determined using mercury intrusion porosimetry.

The petrographic characteristics of the materials were based on analysis of thin sections cut perpendicularly to the outer layers of the samples (optical microscopy in the transmitted polarized light, TPL), using an Olympus BX-51 instrument coupled with an Olympus DP-12 digital camera (Olympus Corporation, Tokyo, Japan). The porosity and pore size distributions were analyzed with a mercury intrusive porosimeter AutoPore IV 9520 (Micromeritics Instrument Corporation, Norcross, GA, USA), operating within the 0.1–413 MPa pressure interval and allowing us to determine pores within the 0.003–1000 μm range.

The morphology of the cement components and microstructure of the materials were studied using a FEI 200 Quanta FEG scanning electron microscope with an EDS/EDAX spectrometer (FEI Company, Fremont, CA, USA). A large number of standardized analysis points were used to characterize residual cement grains and other binder-related phases. The maximum excitation voltage was 20 kV and a low vacuum mode (the pressure 60 Pa) was used. The samples analyzed included polished thin sections, broken, and sharp surfaces of weathered materials, and the efflorescence itself.

Phase compositions of the samples, both of cements and efflorescence, were determined using the X-ray powder diffraction method (XRPD) with a Rigaku MiniFlex 600 instrument (RIGAKU Corporation, Tokyo, Japan). The measurement conditions were as follows: CuKα anode; generator settings 40 kV and 15 mA; recording range 3–70° 2θ; step size 0.05°; counting time 1 sec/step. The results were processed with XRAYAN software using a diffraction X-ray pattern database of the International Centre for Diffraction Data (the Powder Diffraction File PDF-4, 2013).

Some phases, mainly secondary minerals, were also determined using Raman microspectroscopy. The spectra were recorded with a Thermo Scientific DXR Raman microscope (Thermo Scientific, Waltham, MA, USA) with a 900 grooves/mm grating and a CCD detector. The Olympus 10x (NA 0.25) and 50x (NA 0.50) objectives (theoretical spot sizes 2.1 μm and 1.1 μm, respectively) were used. Excitation was activated with a 532 nm diode laser with maximum power of 10 mW. The laser power varied in the 3–10 mW range and the measurement time from 30 to 300 s, selected appropriately to avoid a possible thermal decomposition of the samples and to obtain the best quality of spectra. The phase identification was performed using an in-house and the RRUFF Raman Minerals spectral libraries, as well as the literature data [23–28]. The cement notation used through the paper is as follows: A = Al_2O_3; C = CaO; F = Fe_2O_3; H = H_2O; S = SiO_2.

3. Results and Discussion

3.1. Bright Cement Render at Limestone Blocks above the Pavement Level

Microscopic analysis (TPL) demonstrated that the cement render, covering some of the Pińczów limestone blocks (samples KD-M-4-2), is of a dozen or so millimeters thick, as shown in Figure 2. This outer layer proved to contain fragments of carbonate bioclasts, sharp-edged quartz grains, opaque components, as well as aggregates of high relief that were colorless or colored, mostly isotropic or very slightly anisotropic (very low birefringence) that were difficult to unequivocally identify. Conservation putty, filling the material losses of the limestone blocks, exhibited similar composition. SEM-EDS elemental maps allowed us to identify the presence of Ca, Si, Mg, Al, S, and O, and sometimes Fe as well, as shown in Figure 3. They represent residual cement grains—clinker, that have been identified as alite (C_3S: tricalcium aluminate, $3CaO{\cdot}Al_2O_3$) and belite (C_2S: dicalcium silicate, $2CaO{\cdot}SiO_2$), with the latter predominating, as shown in Table 1 and Figure 4. Although after hydration both alite and belite form hydrated calcium silicates (CSH phases), being the main components of the cements (next to portlandite), these phases can survive in unreacted grains of cements or encapsulated in mortars because of their low hydration rates [5,29].

C_3S exhibits mainly subhedral, rounded, or distorted crystals and often coalescent grains, up to 100 µm in size, as shown in Figure 4a,b. Most of the C_3S grains are corroded and surrounded by partly carbonated hydration rims, as shown in Figure 4a,b. The presence of the silica gel at the boundary can be considered as a weathering product of the cement exposed to atmospheric carbonation. The reaction between C_3S and CO_2, led to the decalcification of C_3S and precipitation of silica gel, which is a residual product of Ca depletion. Belite reveals a diversity of crystal forms and textures. Besides typical, rounded crystals, frequently forming large clusters, atypical, elongated, or wedge-like [30,31] shapes could be observed as well. Rounded crystals, usually of a dozen or so µm in size, or their clusters, up to 100 µm, show polysynthetic twinning, exhibiting one set of parallel lamellae, typical for the type II C_2S (β C_2S) [32], as shown in Figure 4c,d. Belite with two sets of intersecting lamellae (type I, α′ C_2S, [32]) and C_2S not showing any clear lamellae (type III, [33]) were observed only in a few crystals, as shown in Figure 4d. The dominance of β C_2S probably results from the fact that α′-belite is more reactive than the β-belite [5,29]. Several crystals of belite also demonstrate finger-like patterns within the flux phases, as shown in Figure 4a. Although C_2S is generally more stable than C_3S, upon slow cooling, it can reveal reabsorbed finger-like patterns within the interstitial phases [33]. Within the clusters with alite and belite phases, interstitial groundmass composed of hydrated calcium silicate (CSH) occurs. The components are cemented with very fine-crystalline mass, presumably carbonate micrite, which is also indicated by the elemental composition obtained with the SEM-EDS method.

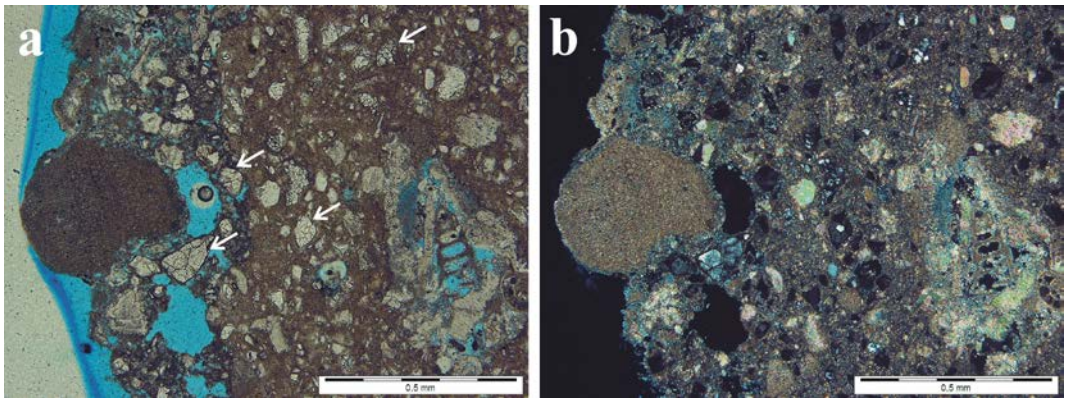

Figure 2. Microphotographs of the sample KD-M-4-2 taken from the wall in places covered and/or filled with bright cement render, above the pavement level; cement clinker clusters are marked with the arrow (one polar (**a**) and crossed polars (**b**)).

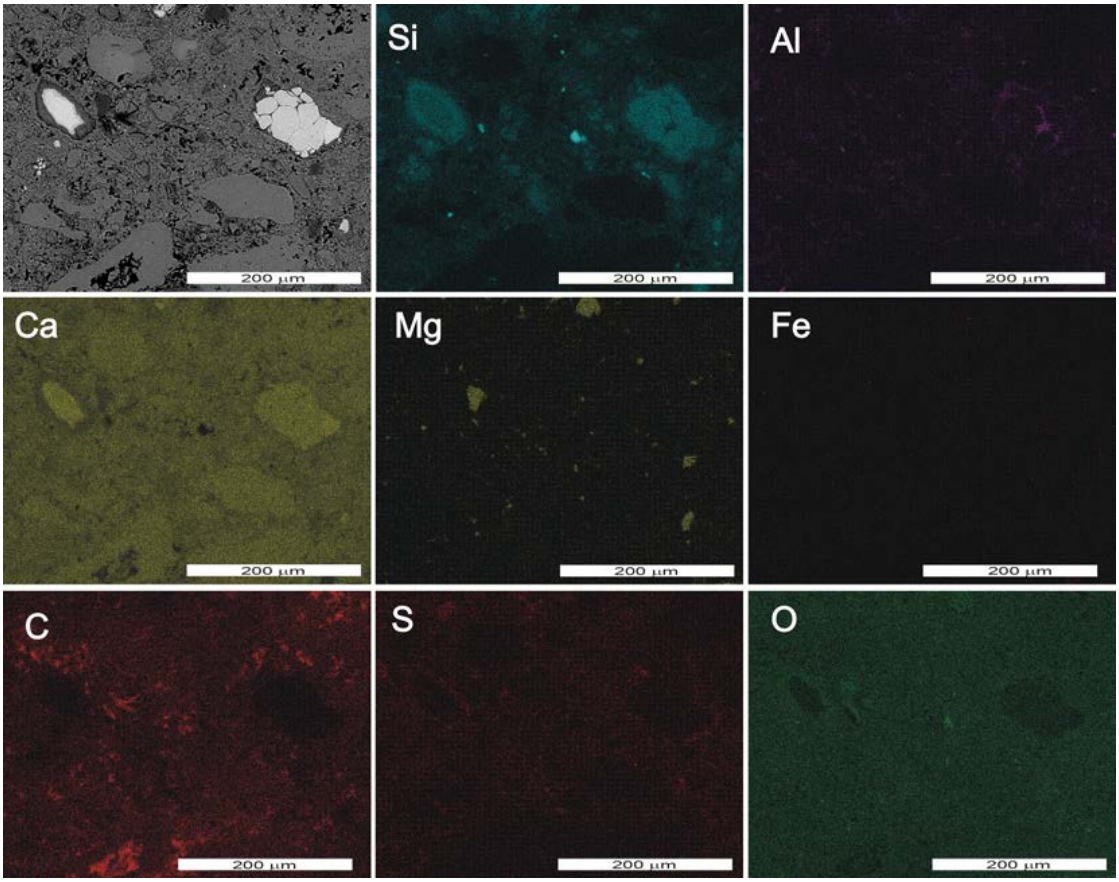

Figure 3. SEM elemental maps and backscattered (BSE) electron image showing the qualitative chemical composition of the cement render with residual cement grains from sample KD-M-4-2.

Table 1. Chemical composition, in atomic percentage, of characteristic residual cement grains. For exact position of the analyzed points, see Figure 4 for the sample KD-M-4-2 and Figure 10 for the sample KD-M-3, discussed in the paragraph 3.2.

Sample	Phase	Analyzed Point	Element							
			O	Na	Mg	Al	Si	Ca	Fe	P
KD-M-4-2										
	C_3S	+1	55.52	0.00	0.47	1.80	10.87	31.34		
	C_2S	+2	56.64	0.00	0.00	0.83	14.33	28.19		
	C_3S	+3	55.86	0.00	0.00	2.14	10.71	31.29		
	C_2S	+4	54.39	0.00	0.00	0.69	14.37	29.95		0.25
	C_2S	+5	56.42	0.00	0.00	0.90	14.04	28.64		
KD-M-3										
	C_3S	+6	56.98	0.00	0.98	1.88	12.40	27.76		
	C_3A	+7	54.12	1.07	0.00	14.33	5.73	23.29	1.46	
	C_4AF	+8	54.99	0.00	1.30	11.06	5.76	20.67	6.23	
	C_2S	+9	57.88	0.00	0.00	1.62	16.12	24.38		
	C_2S	+10	58.14	0.00	0.00	0.70	13.36	27.79		

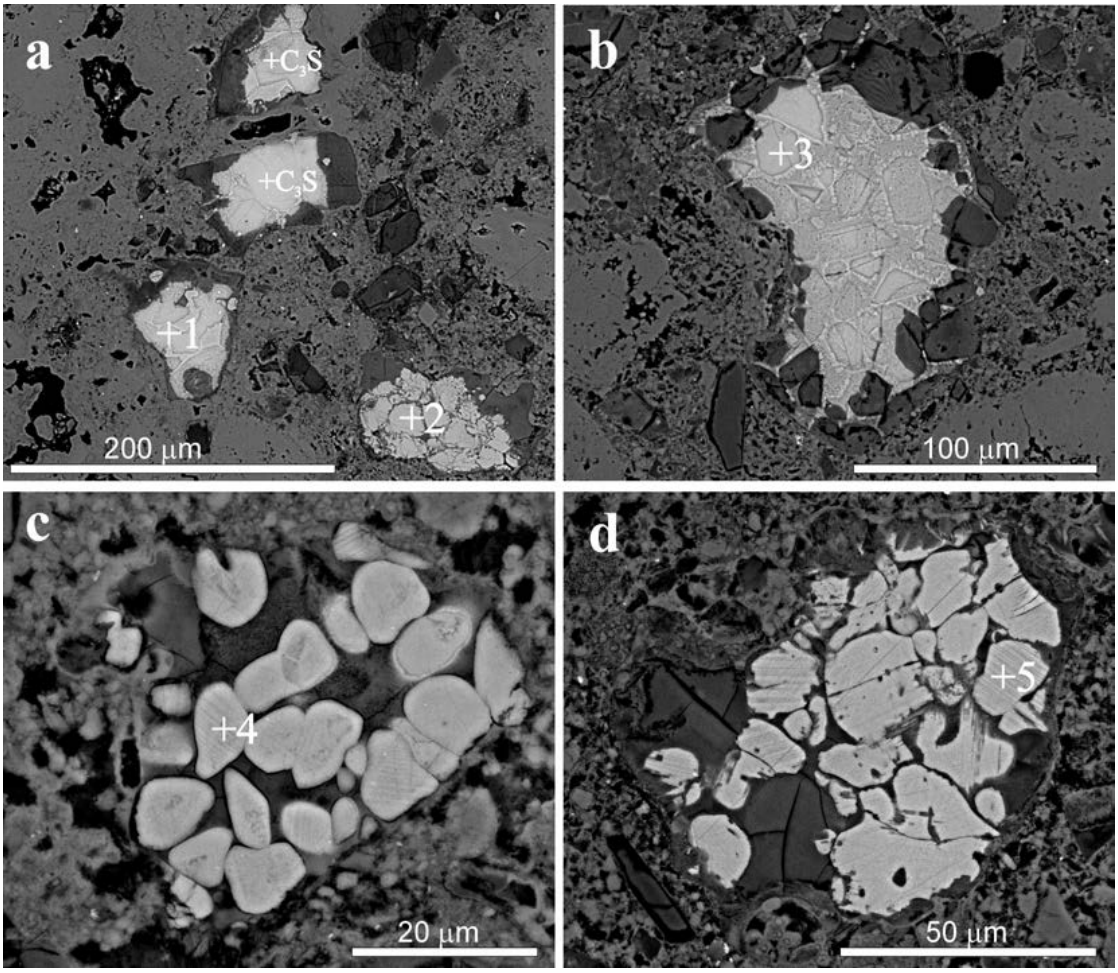

Figure 4. Backscattered (BSE) electron image of residual cement grains from sample KD-M-4-2: (**a**) Grain with coalescent C_3S alite (+1) and belite C_2S, revealing finger-like pattern (+2). The grains are surrounded by rim of inner hydration product; (**b**) Cluster of typical alite crystals (+3) surrounded by silica gel (carbonation product of C_3S); (**c**) Small, rounded belite crystals with parallel lamellae (+4) in a hydrated matrix; (**d**) Subhedral belite crystals type II with lamellae (+5). For qualitative analyses of the phases, see Table 1.

X-ray powder diffractometry (XRPD) allowed us to determine: calcite; portlandite $Ca(OH)_2$; ettringite $Ca_6Al_2(SO_4)_3(OH)_{12}{\cdot}26H_2O$; quartz; dolomite $CaMg(CO_3)_2$; monosulphite $Ca_4Al_2O_6SO_3{\cdot}11H_2O$, as shown in Figure 5. No phases being relics of the original cement, alite and belite, identified through scanning electron microscopy in the binder related grains, were detected using this method.

All these components point out and confirm the use of the Portland cement (PC). Calcium carbonates (calcite as well vaterite) are products of the carbonation of calcium hydroxide (a product of hydration both of C_2S, C_3S, and of lime—CaO, formed after the calcination of raw material, which reacts with CO_2 during the hardening of cement, forming $CaCO_3$). Ettringite is a primary hydration product in ordinary Portland cement (reaction between the calcium aluminate C_3A and the sulphate from added gypsum), but rapidly dissolves after the sulphate depletion. However, this phase can also precipitate when internal (e.g., pyrite) or external sources of sulphate are available (e.g., atmospheric SO_2 [34–36]). The presence of sulfur dioxide in urban and industrial sites mainly promotes the formation of gypsum and ettringite in the pores and the matrix of cementitious materials. Ettringite is thus a product of reaction between gypsum and, still present in the cement, anhydrous grains of calcium aluminates [3]. Depending on the concentration of available sulphates and calcium aluminates (C_3A and tetracalcium aluminoferrite, ferrite C_4AF), crystalizing ettringite generates internal mechanical strength; in particular

conditions (location of ettringite growth, space availability) the high pressure of its crystallization can lead to the damage of the cement matrix. Monosulphite is also a product of the cement hydration (sulphite ions are often observed when sulphuric sources are available; [37,38]).

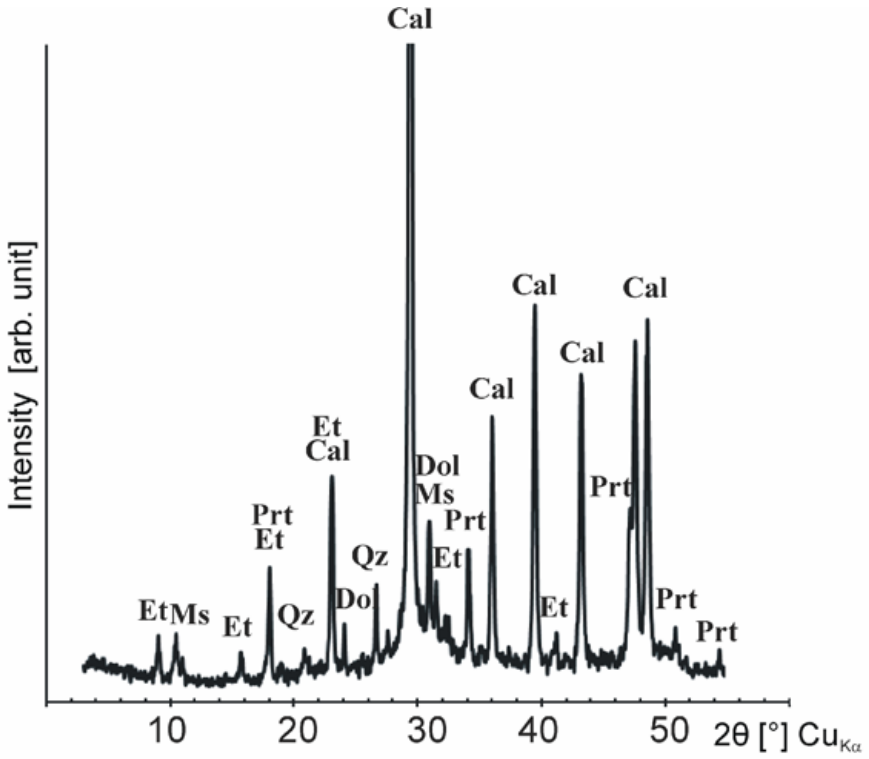

Figure 5. Characteristic X-ray patterns of the cement render of sample KD-M-4-2. Abbreviations: Cal—calcite, Dol—dolomite, Et—ettringite, Ms—monosulphite, Prt—portlandite, Qz—quartz.

The results suggest that the cement render analyzed was based on Portland cement as a binding agent, mixed with crushed stone as an aggregate. In this case it was an organogenic, most probably Pinczów-type limestone with characteristic bioclasts: red algae of the genus Lithothamnium, bryozoans, foraminifers, including genus Amphistegina, and also fragments of bivalve shells.

Based on mercury intrusion porosimetry measurements, the sample reveals a high open porosity of 31.54% and a bulk density of 1.77 g/cm^3. Its pore size distribution reveals a domination of the pores in two ranges: 1.0–0.1 μm, that makes 45.25%, and 0.1–0.003 μm (46.33%). Larger pores of 10.0–1.0 μm make 4.9%, and the pores of 70–10 μm make 3.46%, as shown in Figure 6. The total pore area is 20.31 m^2/g, and the average pore diameter is 0.03 μm (calculated as a weighted average, with the weight determining the number of pores, and not the percentage of the pore space). The internal movement of solutions through the stone is very difficult and inferior (quite high hysteresis effect—45%, and very low threshold diameter—0.5 μm), the permeability is very low 0.075 mD. The pore distribution is unimodal and heterogeneous with the pores in the range 1.0–0.003 μm.

Even though the microscopic analysis (TPL) did not reveal surface coatings with secondary minerals, gypsum on the surface could be observed with the scanning electron microscope. Small, plate-like crystals of this mineral, up to several tens μm in length, were also detected inside the samples analyzed, in pores and cracks, as shown in Figure 7a,b. The formation of gypsum, $CaSO_4 \cdot 2H_2O$, exerts mechanical stress on the stone because of its much higher molecular volume than calcite, $CaCO_3$. Presence of gypsum was confirmed by Raman microspectroscopy. Its spectra show strong Raman bands at 1010 cm^{-1} (ν_1), minor bands at 416 and 492 cm^{-1}, as well as the 621 and 672 cm^{-1} (ν_2 and ν_4) and 1136 cm^{-1} (ν_3) vibrations of SO_4^{2-} [24,27].

Tiny, needle-shaped ettringite crystals were probably dispersed in the matrix, as shown in Figure 3 (distribution of S). Despite the registration of ettringite in the XRPD analyses, no Raman spectra of this mineral have been recognized. It is possible that very fine and disseminated crystals within the matrix were simply not found. Microchemical methods used (e.g., SEM-EDS), do not allow for any unequivocal identification of monosulphite, whose elemental composition is the same as that of ettringite.

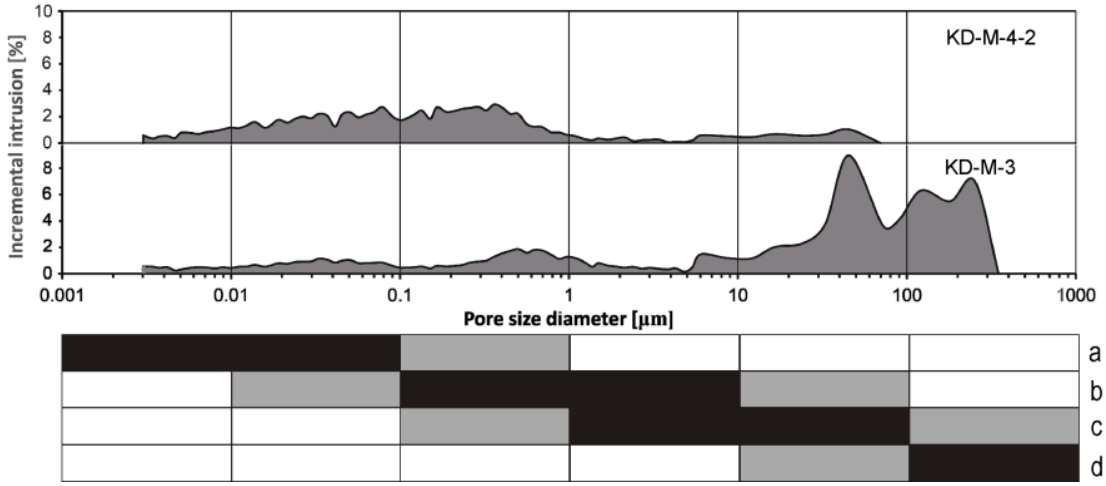

Figure 6. The pore size distribution of the cement based materials (samples KD-M-4-2 and KD-M-3)—for position of the samples, see Figure 1—with regard to certain processes: a—vapor absorption and capillary condensation; b—salt and ice crystallization; c—capillary imbibition; d—mechanical strength in the material pore space. Intensities and ranges of the processes after Benavente [39].

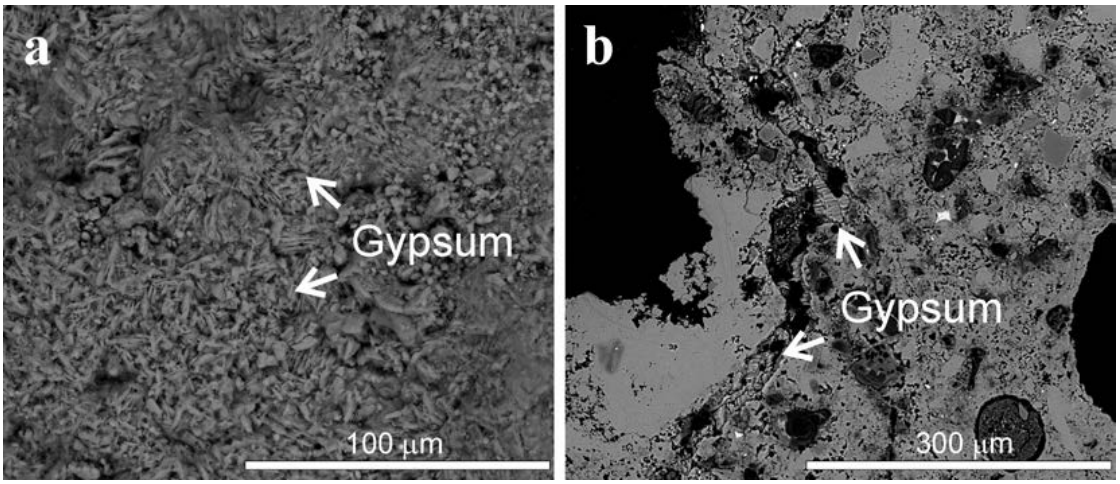

Figure 7. Backscattered (BSE) electron image of the secondary gypsum on the surface (**a**) and in cracks (**b**) of the sample KD-M-4-2.

3.2. Cement Mortar between Stony Blocks of the Subwall below the Pavement Level

In the microscopic image (TPL) cement mortar samples (KD-M-3) display the presence of well-rounded quartz grains, rock fragments, and feldspars (both potassic and plagioclases). These grains are cemented with very fine-grained mass, mainly of Ca, Si, S, and O in composition (SEM-EDS), in which larger yellowish aggregates with high relief, as shown in Figure 8a,b, and low interference colors or even optically isotropic could be observed as well. They represent residual, unhydrated clinker grains of ordinary Portland cement.

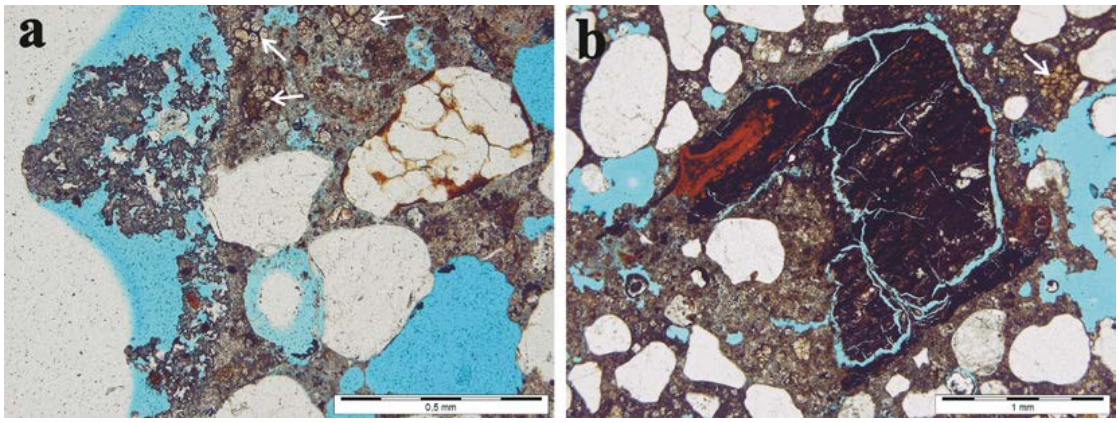

Figure 8. Microphotographs of the cement mortar, sample KD-M–3 taken from the exposed foundations: (**a**) gypsum crust on the surface and cement clinker clusters (marked with the arrow); (**b**) relics of charcoal used as a fuel for the cement burning and residual cement grains (arrow) (plane polarized light).

Their chemical composition is variable; except, aggregates mostly composed of Si, Ca and O, particles, also containing Ca, Al and Fe, could be noted as well, as shown in Table 1 and Figure 9. The analyses allow us to distinguish among them clusters with alite C_3S and belite C_2S, the latter being more abundant than C_3S. Alite crystals are angular, subhedral in shapes, and 10–50 μm in size, as shown in Figure 10a. Typical belite crystals are rounded, a dozen or so micrometers in size, most of them exhibit one set of parallel (type II, β C_2S) or two sets (type I, α′ C_2S) of intersecting lamellae, as shown in Figure 10a,b. Some of the crystals show finger-like shapes, as shown in Figure 10c. Together with alite and belite, interstitial phases, composed of aluminate (C_3A: tricalcium aluminate, $3CaO{\cdot}Al_2O_3$) and ferrite (C_4AF: tetracalcium aluminoferrite, $4CaO{\cdot}Al_2O_3{\cdot}Fe_2O_3$), occur within the clusters, as shown in Figure 10a,c and also in Figure 9. Most of the clusters are around 100 μm in size and surrounded by hydration rims, as shown in Figure 10a,b. The reaction between clinker grains and CO_2 leads to the decalcification of cement relics. The reduction in the Fe content in C_4AF, as shown in Table 1 can be related to weathering processes and/or the substitution of Mg for Fe. The enrichment in Si both C_3A and C_4AF, as shown in Table 1, may result from the isomorphic substitution of Si for Al. These phases are characterized by the more frequent occurrence of substitutions than alite and belite. However, in the case of ferrite, this problem may be more complex and related to the specific distribution of Fe and Al atoms in the Ca_2FeAlO_5 structure, as they could be located in octahedral or tetrahedral layers (about 75% of octahedral and tetrahedral sites are occupied by Fe and Al, respectively). This implies a mixed substitution of Mg for both Fe and Al and similarly of Si for Al and Fe, but with a preference according to the order give (i.e., Mg for Fe and Si for Al; [40,41]).

Relics of charcoal used as a fuel for the cement burning were also found, as shown in Figure 8b.

The XRPD analysis of the cement mortar samples revealed only quartz, calcite, feldspars, and gypsum. Neither C_3S, C_2S, C_4AF, nor C_3A were detected with this method.

The sample displays an open porosity of 18.33% and a bulk density of 2.08 g/cm^3. Its pore size distribution indicates the pores in the ranges: 350–10 μm that makes 44.8%, 1.0–0.1 μm that makes 22.9%, and the pores of 0.1–0.003 μm (21.5%). The pores of 10.0–1.0 μm make 10.8%, as shown in Figure 6. The average pore diameter (calculated as a weighted average, with the weight determining the number of pores and not the percentage of the pore space) is of 0.06 μm, and the total pore area is 5.69 m^2/g. The quite low hysteresis effect (28%) and threshold diameter (50 μm) indicate that the internal movement of solutions through the material is easy and the permeability is 8.96 mD.

In places, the surface of the cement mortar samples is coated with a discontinuous layer with tiny, plate-shaped almost isotropic components, opaque grains, and sharp-edged iron oxides, as shown in Figure 8a, apparently formed due to exposition in the polluted atmosphere. Main components of that crust are calcium sulphates (mostly gypsum), also found deeper in the sample. The pore

size distribution distinctly points out susceptibility to salt crystallization in the pores of the material investigated, as shown in Figure 6. Gypsum occurs as small plate-like crystals, mostly up to several tens μm in length, sometimes accumulating on the surface in the form of rosettes, as shown in Figure 11a. The presence of gypsum was verified by Raman microspectroscopy, based on the bands: strong band at 1010 cm^{-1} (ν_1), minor bands at 416 and 492 cm^{-1} and also at 621 and 672 cm^{-1} (ν_2 and ν_4), and 1136 cm^{-1} (ν_3) vibrations of SO_4^{2-}, as shown in Figure 12a [24,27].

Efflorescences could be observed on the border between the limestone blocks and the cement mortar. The XRPD analyses allowed us to identify sulphates—thenardite Na_2SO_4, aphthitalite (glaserite) $(K,Na)_3Na(SO_4)_2$—and sulphate–nitrate salt—darapskite $Na_3(SO_4)(NO_3)\cdot H_2O$. The remaining components—calcite and quartz, are mostly related to the underlying material, as shown in Figure 13.

Thenardite reveals characteristic euhedral (bipyramidal) crystals composed of Na, S, and O with sizes not exceeding 20 μm in length, as shown in Figure 11b. The identification of this mineral has been based on its Raman spectrum, as shown in Figure 12b: main band at 990 cm^{-1} (ν_1 SO_4^{2-}), set of bands at 449, 460 cm^{-1} (ν_2 SO_4^{2-}), and 617, 629, 643 cm^{-1} (ν_4 SO_4^{2-}), and also other bands at 1099, 1128 and 1149 cm^{-1} (ν_3 SO_4^{2-}) [28]. Nevertheless, the presence of decahydrous mirabilite $Na_2SO_4\cdot 10H_2O$ is also possible. At RH > 76,4% mirabilite predominates, but with an increase in the temperature and a decrease in the humidity, it turns to thenardite [25,42]. However, distinguishing mirabilite from thenardite in Raman spectroscopy could be ambiguous because of the close positions of their main Raman bands [25,28]. Salts, which can crystallize as various hydrates are particularly damaging. For the volumometric changes in reversible, dissolving/recrystallizing processes in the case of anhydrous thenardite, decahydrous mirabilite even reaches 314%, and a stone damage results just from the crystallization pressure generated in their course [43].

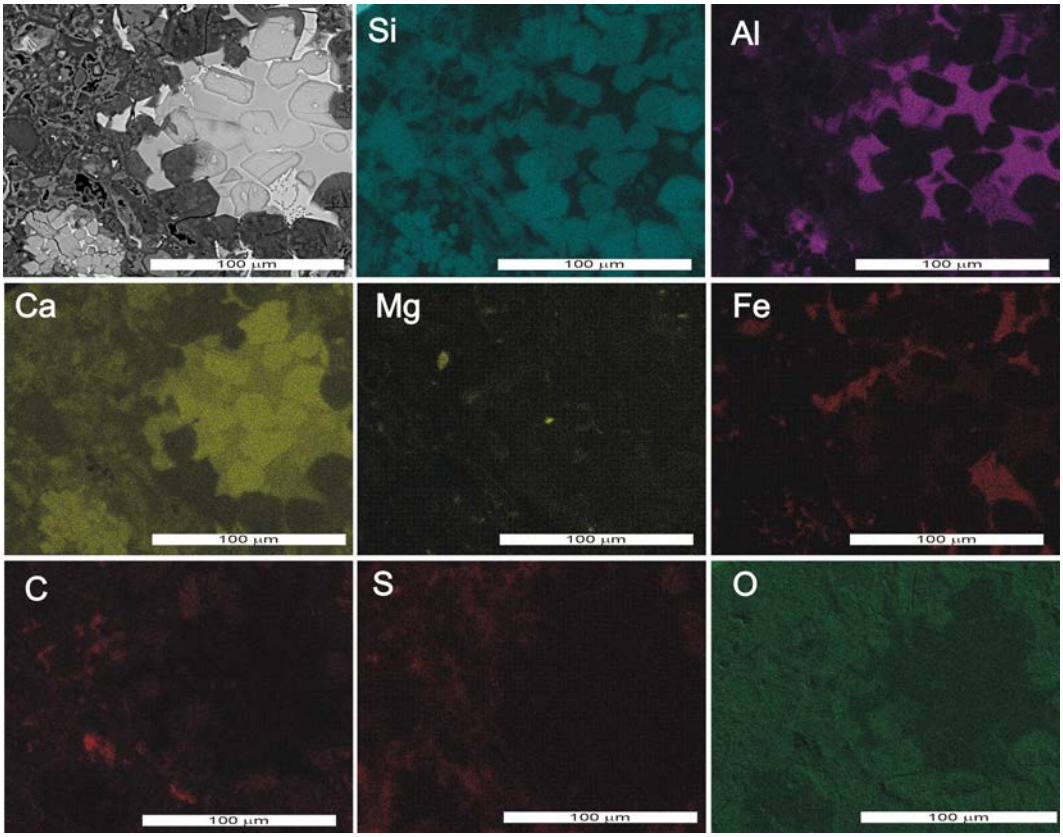

Figure 9. SEM elemental maps and backscattered (BSE) electron image showing the qualitative chemical composition of the cement mortar with residual cement grains for sample KD-M-3.

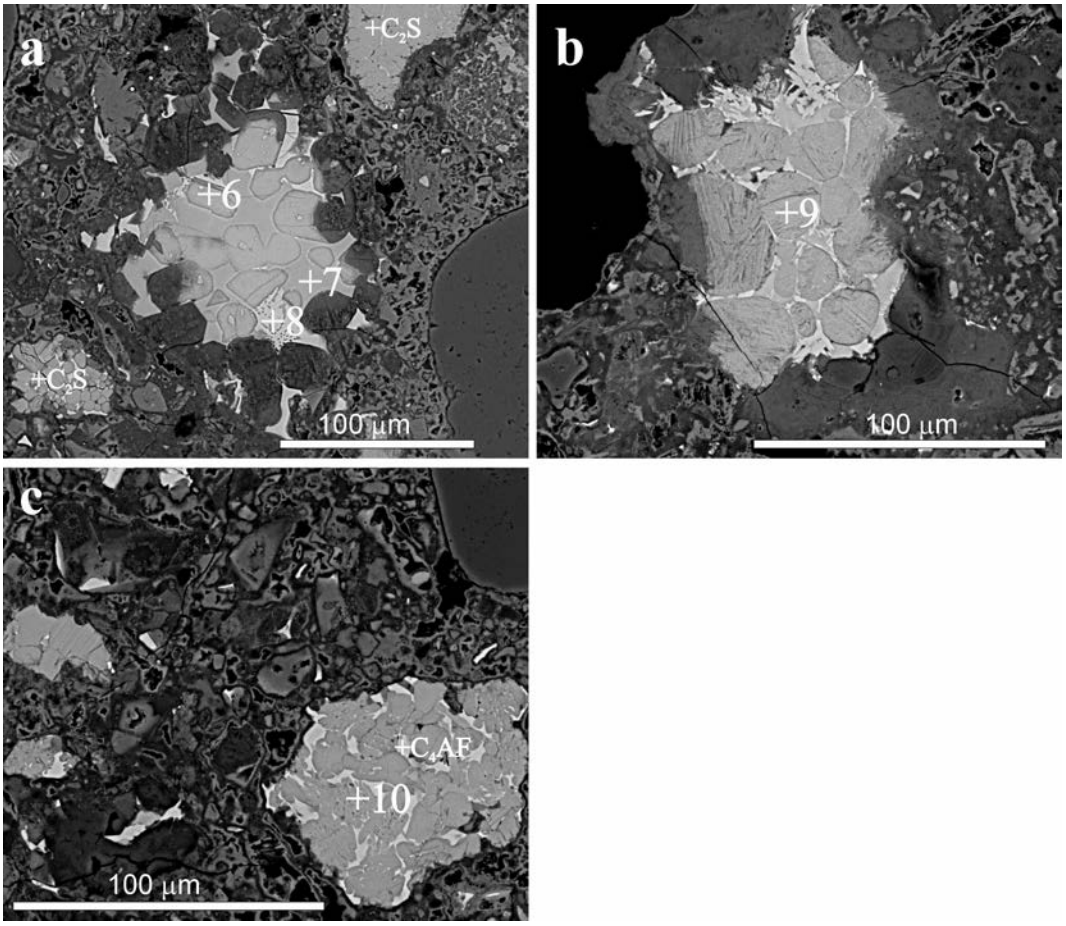

Figure 10. Backscattered (BSE) electron image of residual cement grains from sample KD-M-3: (**a**) elongated, angular crystals of alite C_3S (+6) in an aluminate C_3A (+7) and ferrite C_4AF (+8) matrix; (**b**) cluster of belite C_2S type I with two sets of intersecting lamellae (+9) in ferrite matrix, surrounded by hydrated rim; (**c**) finger-shaped belite crystals (+10) in ferrite matrix. For qualitative analyses of the phases, see Table 1.

Both double salts—aphthitalite $(K,Na)_3Na(SO_4)_2$ and darapskite $Na_3(SO_4)(NO_3)\cdot H_2O$—display a complex crystallization behavior and may be highly damaging for building materials [44,45]. They are incongruently soluble; that is, under equilibrium conditions, these compounds do not crystallize from a solution of their own stoichiometric compositions [44,45].

Aphthitalite $(K,Na)_3Na(SO_4)_2$, in EDS analyses revealing the presence of Na, K, S and O, occurs in the form of anhedral, often isometric crystals and irregular aggregates, as shown in Figure 11c. Its Raman spectra exhibited a strong band at 986 cm^{-1}, assigned to the ν_1 symmetric stretching mode of the sulphate group, and the bands at 449 (ν_2), 1082 (ν_3), and 1203 cm^{-1}, as shown in Figure 12c. The presence of a band at ~1202 cm^{-1} and the lack of band at 465 cm^{-1} allows us to distinguish sodium and potassium sulphate—aphthitalite and anhydrous sodium sulphate—thenardite that have very similar Raman spectra, and both of them appear in the efflorescence analyzed [23,28].

Euhedral, platy crystals of various length, up to several tens µm, sometimes fan-shaped, consisting of Na, S, and O, are most likely darapskite $Na_3(SO_4)(NO_3)\cdot H_2O$, as shown in Figure 11d. The Raman spectra confirm the presence of this mineral without any doubt. The spectra exhibit strong bands at 1060 cm^{-1} and 992–989 cm^{-1} of ν_1 NO_3^- and ν_1 SO_4^{2-}, respectively, as shown in Figure 12d. The bands at 452 can be assigned to ν_2 SO_4^{2-}; 728 and 706 cm^{-1} to ν_4 SO_4^{2-} and ν_4 NO_3^-, accordingly; 640 and 617 cm^{-1} to ν_4 SO_4^{2-}. Weak signals at 1123 and 1083 cm^{-1} are connected with ν_3 SO_4^{2-}, and those at 1353 cm^{-1} with ν_3 NO_3^- [26].

Aphthitalite can crystallize from mixtures containing solutions of sodium sulphate—Na_2SO_4 and potassium sulphate—K_2SO_4. Darapskite is a mineral of the system Na_2SO_4–$NaNO_3$–H_2O. Founded in the efflorescence analyzed, both aphthitalite and darapskite suggest a more complex system of solutions; that is, containing K_2SO_4–Na_2SO_4–$NaNO_3$–H_2O. According to the solubility data, aphthitalite should precipitate as the first upon evaporation of an equimolar mixed solution of sodium sulphate—Na_2SO_4 and potassium sulphate—K_2SO_4 [46]. Darapskite is stable between 13.5 and 74 °C and can never occur together with nitratine $NaNO_3$ and thenardite/mirabilite, because the stability fields of the latter two are separated by the darapskite field [47,48]. However, in the efflorescence analyzed, thenardite and darapskite occur together. According to the solubility diagram of the Na_2SO_4–$NaNO_3$–H_2O system at 20 °C [44], as water evaporates, the concentration of these two salts increases, first reaching saturation with mirabilite. The remaining solution becomes enriched in nitrate, and then also gets saturated with darapskite. In the equilibrium conditions mirabilite will re-dissolve and darapskite will crystallize instead. However, in porous materials, the re-dissolution of mirabilite may not occur, as the evaporation front moves inside, and the precipitated mirabilite will be separated from the solution. The latter will then first precipitate darapskite and, in the end, nitratine. Nitrate salts—nitratine $NaNO_3$ and nitre KNO_3—have been detected on the surface of the Jurassic limestone in the vicinity of the efflorescence [20].

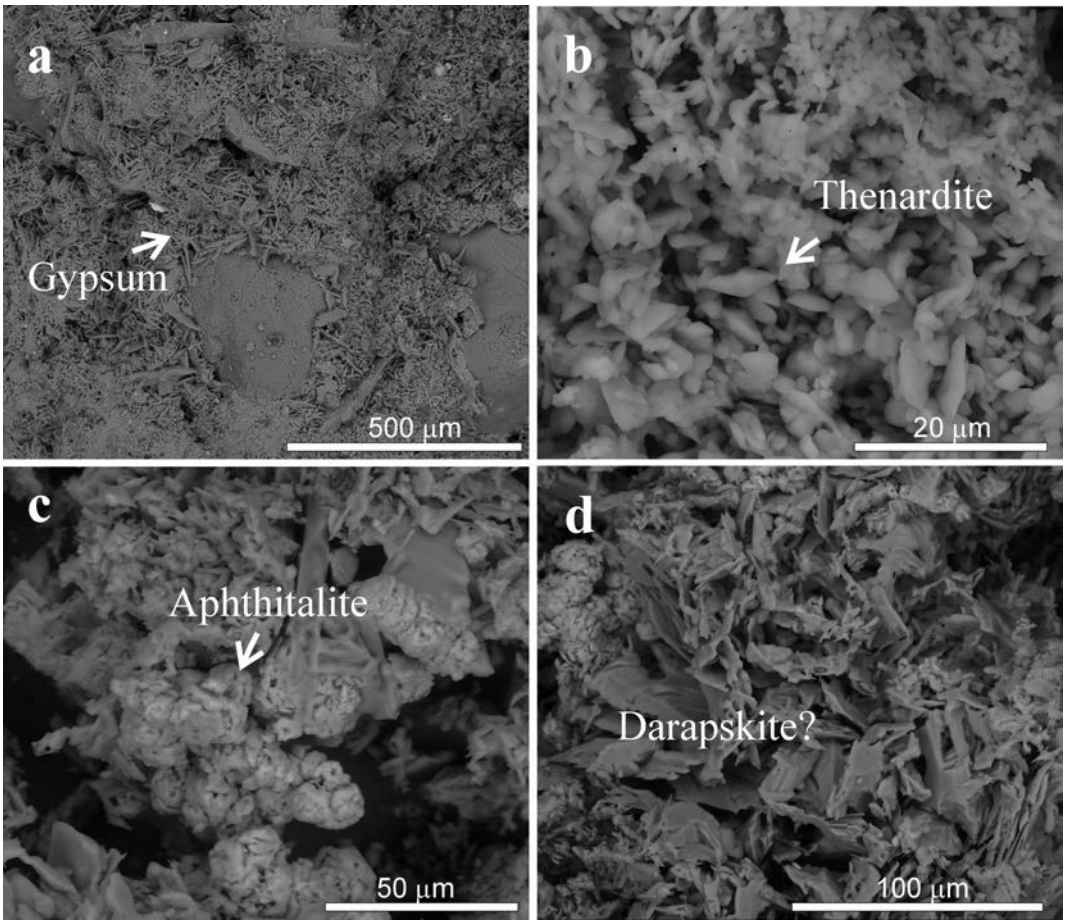

Figure 11. Backscattered (BSE) electron image of the secondary salts from the crust of the sample KD-M-3 (**a**) and from the efflorescence at the border between the subwall limestone blocks and cement mortar (**b**–**d**).

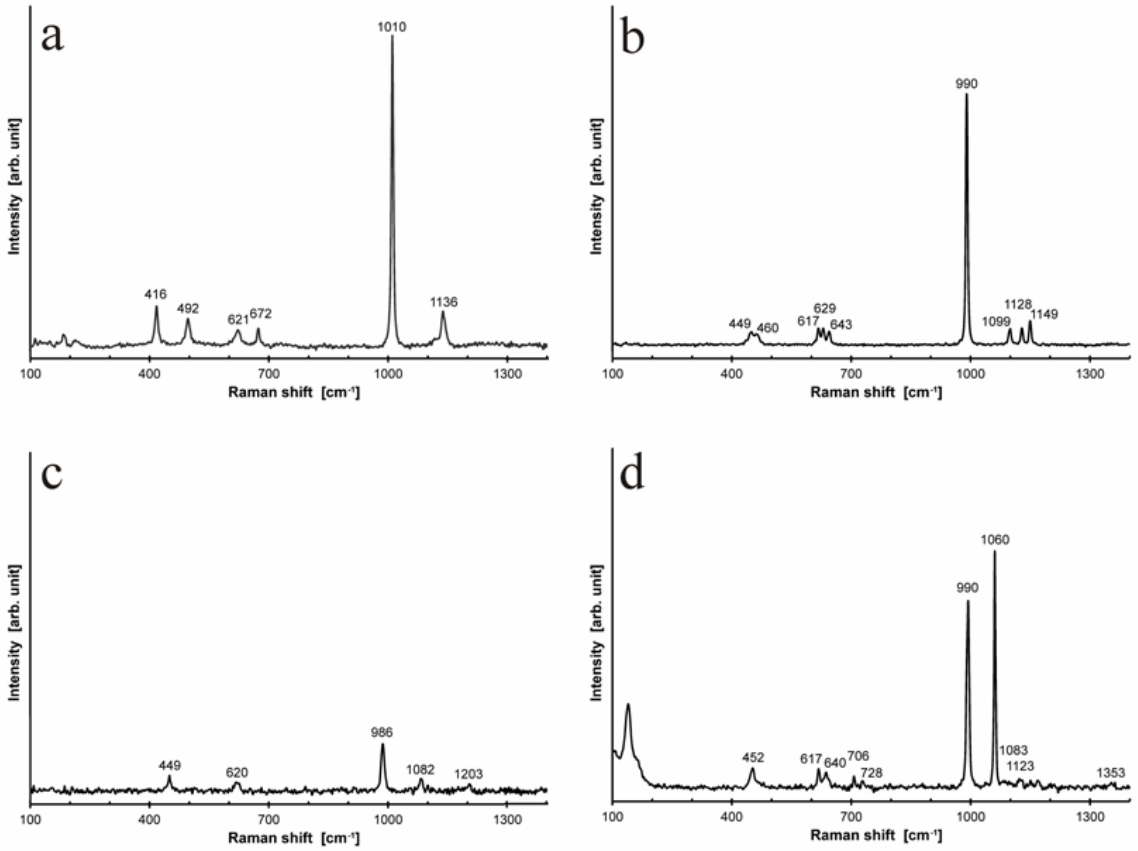

Figure 12. Representative, characteristic Raman spectra of the secondary salts: gypsum from the cement mortar crust (**a**) and efflorescence at the border between the subwall limestone blocks and cement mortar: thenardite (**b**); aphthitalite (**c**); darapskite (**d**).

The ions of crystallized sodium, potassium, calcium sulphate, and sulphate–nitrate salts may come from both internal and external sources—natural and anthropogenic ones. The internal sources of the ions are mainly weathering and leaching cement components, but also in the adjacent stone blocks (sandstones and limestones) of the foundations exposed. The domination of sodium and potassium salts in the efflorescence (thenardite/mirabilite, darapskite, and aphthitalite) implies that these cations could migrate from both cement mortar and sandstone blocks (Na and K released from weathering feldspars, micas, and clay minerals). Although the information on previous conservation works cannot be verified, their contribution seems to be very likely. Materials used at the conservation, such as water glass, could yield Na and Ca (Ca regarding gypsum) ions [49,50].

The analysis of the external anthropogenic sources should start from the air pollution—wet and dry airborne deposition supplying mainly sulphate and nitrate anions. The road de-icing salts (NaCl and $CaCl_2$) and detergent solutions used for cleaning (e.g., streets) could be sources of both Na and Ca cations and also chloride ions. Halite was observed at various elements of the chapel façade and foundations [20]. The position of the foundations below the pavement level, adjacently to the drying ditch, exposing subwall, promotes the movement of these substances to the foundations. Other extrinsic sources of ions for precipitated salts could be animal (e.g., droppings of birds, such as pigeons in Cracow) and microbiological activities, as well as capillary rises in ground and soil waters.

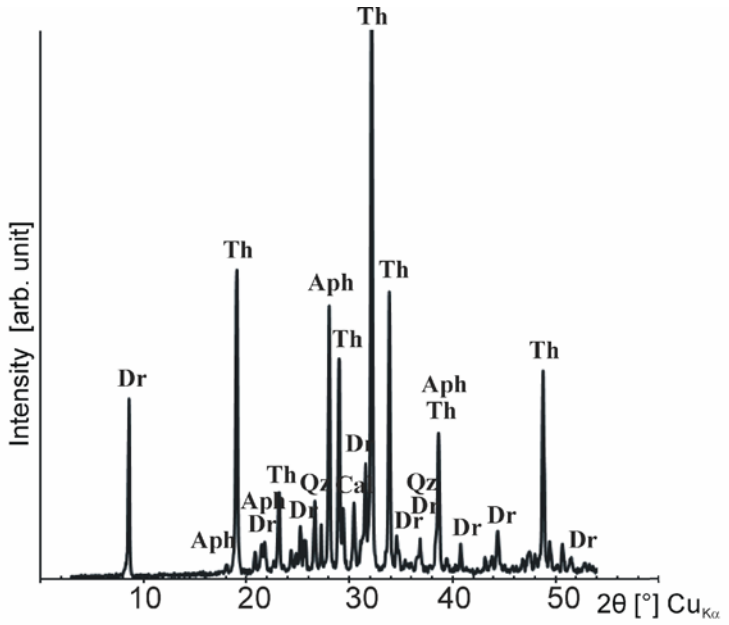

Figure 13. Characteristic X-ray patterns of the efflorescence sampled from the border between the subwall limestone blocks and cement mortar. Abbreviations: Aph—aphthitalite, Cal—calcite, Dr—darapskite, Th—thenardite, Qz—quartz.

Although since the 1990s the concentration of pollution in Cracow has been decreasing, the level of gaseous and particulate pollution is still significant [51,52]. This is a consequence of the unfavorable atmospheric conditions of the town, which include weak winds, temperature inversions, fogs [53], as well as the presence of large industrial centers and fossil fuel burning. Additionally, road transport contributes its share, notably in the dense structural layout of the Cracow Old Town. Industrial emissions, carried by prevailing western winds from neighbouring regions, further increases the pollution level in the city.

4. Conclusions

The study presents characteristics of the cement render and mortar used for stone repair and/or substitution at the Myszkowskis chapel of the Holy Trinity Church in Cracow. The analyses demonstrated that the render covering some of the decayed Pińczów limestone blocks of the chapel façade was prepared using Portland cement as a binding agent, mixed with crushed stone as an aggregate. Characteristic bioclasts—red algae of the genus Lithothamnium, bryozoans, foraminifers, broken pieces of bivalve shells—point out an organogenic limestone of the Pińczów type. The relics of the PC clinker detected include unhydrated alite C_3S and belite C_2S crystals of various morphology and texture in the form of clusters, often with rims of inner hydration products. The main components of the cement, in addition to portlandite $Ca(OH)_2$, are ettringite $Ca_6Al_2(SO_4)_3(OH)_{12}{\cdot}26H_2O$, monosulphite $Ca_4Al_2O_6SO_3{\cdot}11H_2O$, and gypsum. Although ettringite is a primary hydration product in ordinary Portland cement, it rapidly dissolves when the sulphate, generally gypsum added to the PC, is exhausted. This phase, however, precipitates again with the availability of an external source of sulphate (e.g., air pollution sulfur dioxide, still abundant in Cracow). In the case studied, the secondary gypsum, observed on the surface and in the cracks of the render, presents such a sulphate source, allowing ettringite and monosulphite to precipitate. Moreover, the C_3A and C_4AF substrates needed to form these sulphates have not been observed, either within the clusters of C_2S and C_3S, or in the cement matrix. This may suggest their exhaustion due to the sulphate crystallization and seems to support this supposition. The crystallization of ettringite, monosulphite, and gypsum undoubtedly damaged the render used for the stone repair and/or substitution.

The cement mortar between stony blocks of the subwall below the pavement level was based on the Portland cement mixed with aggregate containing quartz, feldspars, and rock fragments. The relics of unhydrated PC clinker include alite C_3S and belite C_2S clusters with aluminate C_3A and ferrite C_4AF as interstitial phases within the clusters. The main components of the cement mortar analyzed are calcite, quartz, feldspars, and gypsum. The following hydrated secondary salts have been detected: simple salts—except gypsum $CaSO_4{\cdot}2H_2O$ thenardite/mirabilite $Na_2SO_4/Na_2SO_4{\cdot}10H_2O$; a double sodium/potassium salt—aphthitalite $(K,Na)_3Na(SO_4)_2$; a double sulphate/nitrate salt—darapskite $Na_3(SO_4)(NO_3){\cdot}H_2O$. Gypsum, in the form of crusts, was observed on the mortar surface. The sulphate and sulphate/nitrate salts of sodium and potassium—thenardite/mirabilite, aphthitalite and darapskite—are present in the form of efflorescence (in some parts of the foundations). The high porosity and capillary of the cement matrix promote the salt migration and allow the salt crystallization at the interface cement/stone. The compositions of the salts are mostly related to the components of the cement mortar in replacements and joints, but it may be affected by the sandstone blocks and possible past conservation materials as well. The secondary sulphate and sulphate/nitrate salts reported are related to the air pollution in Cracow as well. More accurate characteristics of different sources of sulphates would require sulfur and oxygen stable isotope analyses.

Author Contributions: M.M. conceived the idea, performed most of the measurements and interpreted the result, wrote the manuscript, and prepared most of the figures; K.D. assisted with the OM analyses and helped to improve the English version of the manuscript; A.G. performed XRPD analyses and prepared some of the figures. All authors have read and agreed to the published version of the manuscript.

Funding: The studies were supported by the AGH University of Science and Technology, Kraków, grant 16.16.140.315.

Acknowledgments: The authors acknowledge the help of B. Polczyński and K. Bałaga in sampling the historic monument and G. Machowski, E. Pstrucha and A. Pstrucha from the Mercury Porosimetry Laboratory, AGH-UST, for performing mercury porosimetry measurements. We would like to thank both anonymous reviewers for their comments, which were helpful in improving the manuscript.

Conflicts of Interest: The authors declare no conflict of interest.

References

1. Snethlage, R.; Sterflinger, K. Stone Conservation. In *Stone in Architecture*; Siegesmund, S., Snethlage, R., Eds.; Springer: Berlin/Heidelberg, Germany, 2011; pp. 411–544. [CrossRef]
2. Adamski, G.; Bratasz, L.; Kozlowski, R.; Mayr, N.; Mucha, D.; Stilhammerova, M.; Weber, J. Roman cement—Key historic material to cover the Exteriors of buildings. In *RILEM Workshop Repair Mortars for Historic Masonry*; Groot, C., Ed.; RILEM Publications SARL: Paris, France, 2009; pp. 2–11.
3. Gosselin, C.; Verges-Belmin, V.; Royer, A.; Martinet, G. Natural cement and monumental restoration. *Mater. Struct.* **2009**, *42*, 749–763. [CrossRef]
4. Kozłowski, R.; Hughes, D.; Weber, J. Roman Cements: Key Materials of the Built Heritage of the 19th Century. In *Materials, Technologies and Practice in Historic Heritage Structures*; Bostenaru Dan, M., Přikryl, R., Török, A., Eds.; Springer: Dordrecht, The Netherlands, 2010; pp. 259–277. [CrossRef]
5. Pintér, F.; Gosselin, C. The origin, composition and early age hydration mechanisms of Austrian natural Portland cement. *Cem. Concr. Res.* **2018**, *110*, 1–12. [CrossRef]
6. Bartz, W.; Filar, T. Mineralogical characterization of rendering mortars from decorative details of a baroque building in Kożuchów (SW Poland). *Mater. Charact.* **2010**, *61*, 105–115. [CrossRef]
7. Szeląg, H.; Garbacik, A.; Pichniarczyk, P.; Baran, T. Roman cement and its properties. *Surow. Masz. Bud.* **2008**, *1*, 74–78. (In Polish)
8. Szeląg, H.; Garbacik, A.; Pichniarczyk, P.; Baran, T. Contemporary Roman cement and its properties. *Bud. Czas. Tech. Wydaw. Politech. Krak.* **2009**, *109*, 337–345. (In Polish with English Abstract)
9. Weber, J.; Gadermayr, N.; Kozłowski, R.; Mucha, D.; Hughes, D.; Jaglin, D.; Schwarz, W. Microstructure and mineral composition of Roman cements produced at defined calcination conditions. *Mater. Charact.* **2007**, *58*, 1217–1228. [CrossRef]

10. Kloppmann, W.; Bromblet, P.; Vallet, J.M.; Vergès-Belmin, V.; Rolland, O.; Guerrot, C.; Gosselin, C. Building materials as intrinsic sources of sulphate: A hidden face of salt weathering of historical monuments investigated through multi-isotope tracing (B, O, S). *Sci. Total Environ.* **2011**, *409*, 1658–1669. [CrossRef]
11. Prikryl, R.; Weishauptova, Z.; Novotna, M.; Prikrylova, J.; St'astna, A. Physical and mechanical properties of the repaired sandstone ashlars in the facing masonry of the Charles Bridge in Prague (Czech Republic) and an analytical study for the causes of its rapid decay. *Environ. Earth Sci.* **2011**, *63*, 1623–1639. [CrossRef]
12. Morillas, H.; Maguregui, M.; Trebolazabala, J.; Madariaga, J.M. Nature and origin of white efflorescence on bricks, artificial stones, and joint mortars of modern houses evaluated by portable Raman spectroscopy and laboratory analyses. *Spectrochim. Acta Part A* **2015**, *136*, 1195–1203. [CrossRef]
13. Flatt, R.J.; Steiger, M.; Scherer, G.W. A commented translation of the paper by C.W. Correns and W. Steinborn on crystallization pressure. *Environ. Geol.* **2007**, *52*, 187–203. [CrossRef]
14. Bieniarzówna, J.; Małecki, J.M. *The History of Cracow, Volume 2, Cracow in the 16th–18th Centuries*; Wydawnictwo Literackie: Kraków, Poland, 1984; 670p. (In Polish)
15. Dobrowolski, T. *Art of Cracow*, 5th ed.; Wydawnictwo Literackie: Kraków, Poland, 1978; 623p. (In Polish)
16. Rożek, M. *Urbs Celeberrima. Cracow Monuments Guide*; WAM: Kraków, Poland, 2009; 624p. (In Polish)
17. Grabski, W.; Nowak, J. *Technological and Mineralogical-Petrographic Studies on the Pińczów Limestone (Symptoms and Causes of Stone Destruction at the Dome of the Myszkowskis Chapel of the Dominican Order Church in Cracow)*; No inv.3126/77; Archive of Cracow City Office, Department of Conservation of Monuments: Kraków, Poland, 1960; p. 26. (In Polish, Manuscript)
18. Rajchel, J. *Stony Cracow*; Uczelniane Wydawnictwa Naukowo-Dydaktyczne AGH: Kraków, Poland, 2004; p. 235. (In Polish)
19. Grabski, W.; Nowak, J. The Problem of stone destruction in the historic buildings of Cracow. *Mater. Bud.* **1957**, *1*, 33–39. (In Polish)
20. Marszałek, M.; Dudek, K.; Gaweł, A.; Czerny, J. Mineralogical and geochemical studies of secondary mineral assemblages related to deterioration of building materials. *Geol. Q.* **2019**, *63*, 683–698. [CrossRef]
21. Górecki, J.; Sermet, E. Quarries of Cracow—The heritage underestimated. In *Mining History—An Element of the European Cultural Heritage*; Zagożdżon, P.P., Madziarz, M., Eds.; Oficyna Wydawnicza Politechniki Wrocławskiej: Wrocław, Poland, 2010; Volume 3, pp. 123–138. (In Polish)
22. Bochnak, A.; Samek, J. *Katalog Zabytków Sztuki w Polsce. Tom IV Miasto Kraków. Kościoły i Klasztory Śródmieścia, 2*; Instytut Sztuki Polskiej Akademii Nauk: Warszawa, Poland, 1978; 256p.
23. Hansteen, E.T.; Burke, E. Aphthitalite in hight-temperature fluid inclusions in quartz from Eikeren-Skrim granite complex, the Oslo paleorift. *Nor. Geol. Tidsskr.* **1994**, *74*, 238–240.
24. Buzgar, N.; Buzatu, A.; Sanislav, I.V. The Raman study on certain sulfates. *An. Ştiinţ. Univ. "Al.I. Cuza"* **2009**, *55*, 5–23.
25. Hamilton, A.; Menzies, R.I. Raman spectra of mirabilite, $Na_2SO_4{\cdot}10H_2O$ and the rediscovered metastable heptahydrate, $Na_2SO_4{\cdot}7H_2O$. *J. Raman Spectrosc.* **2010**, *41*, 1014–1020. [CrossRef]
26. Jentzsch, P.V.; Ciobota, V.; Kampe, B.; Rösch, P.; Popp, J. Origin of salt mixtures and mixed salts in atmospheric particulate matter. *J. Raman Spectrosc.* **2012**, *43*, 514–519. [CrossRef]
27. Prieto-Taboada, N.; Gómez-Laserna, O.; Martínez-Arkarazo, I.; Olazabal, Á.M.; Madariaga, J.M. Raman Spectra of the Different Phases in the $CaSO_4$–H_2O System. *Anal. Chem.* **2014**, *86*, 10131–10137. [CrossRef] [PubMed]
28. Prieto-Taboada, N.; Fdez-Ortiz de Vallejuelo, S.; Veneranda, M.; Lama, E.; Castro, K.; Arana, G.; Larrañaga, A.; Madariaga, J.M. The Raman spectra of the Na_2SO_4 -K_2SO_4 system: Applicability to soluble salts studies in built heritage. *J. Raman Spectrosc.* **2019**, *50*, 175–183. [CrossRef]
29. Pintér, F.; Vidovszky, I.; Weber, J.; Bayer, K. Mineralogical and microstructural characteristics of historic Roman cement renders from Budapest, Hungary. *J. Cult. Herit.* **2014**, *15*, 219–226. [CrossRef]
30. Ando, Y.; Hirono, S.; Sawaki, D.; Katayama, T. Microscopy to evaluate the properties of cement and alterations in historic mortar/concrete of old Nobiru Port project, Northeast Japan. In Proceedings of the 36th ICMA Conference, Milan, Italy, 13–17 April 2014; pp. 212–233.
31. Katayama, T.; Ando, Y.; Hirono, S.; Sawaki, D.; Itoga, H. Relicts of unhydrated cement clinker in a historic concrete from the 19th century—Microscopy with EDS analysis of old training dyke at Yokohama port, Japan. In Proceedings of the 36th ICMA Conference, Milan, Italy, 13–17 April 2014; pp. 432–458.

32. Insley, H. Structural characteristics of some constituents of Portland cement clinker. *J. Res. Natl. Bur. Stand.* **1936**, *17*, 353–361. [CrossRef]
33. Campbell, D.H. *Microscopical Examination and Interpretation of Portland Cement and Clinker*, 2nd ed.; Portland Cement Association: Skokie, IL, USA, 1999; p. 214.
34. Sabbioni, C.; Zappia, G.; Riontino, C.; Blanco-Varela, M.T.; Aguilera, J.; Puertas, F.; Van Balen, K.; Toumbakari, E.E. Atmospheric deterioration of ancient and modern hydraulic mortars. *Atmos. Environ.* **2001**, *35*, 539–548. [CrossRef]
35. Gosselin, C.; Girardet, F.; Feldman, S.B. Compatibility of Roman cement mortars with gypsum stones and anhydrite mortars: The example of Valère Castle (Sion, Switzerland). In Proceedings of the 12th International Congress on the Deterioration and Conservation of Stone, New York, NY, USA, 21–25 October 2012; Columbia University: New York, NY, USA, 2012; pp. 1–11.
36. Gosselin, C.; Scrivener, K.L.; Feldman, S.B.; Schwarz, W. The hydration of modern roman cements used for current architectural restoration. In *Historic Mortars: Characterisation, Assessment and Repair*; RILEM Book Series, 7, Valek, J., Hughes, J.J., Groot, C.J.W.P., Eds.; Springer: Dordrecht, Holland, 2012; pp. 297–308. [CrossRef]
37. Łagosz, A.; Małolepszy, J. Tricalcium aluminate hydration in the presence of calcium sulfite hemihydrates. *Cem. Concr. Res.* **2003**, *33*, 333–339. [CrossRef]
38. Suh, J.; Sung Yumb, W.; Jeong, Y.; Park, H.G.; Eun Oh, J. The cation-dependent effects of formate salt additives on the strength and microstructure of CaO-activated fly ash binders. *Constr. Build. Mater.* **2019**, *194*, 92–101. [CrossRef]
39. Benavente, D. Why pore size is important in the deterioration of porous stones used in the built heritage. *MACLA* **2011**, *15*, 41–42.
40. Tao, Y.; Zhang, W.; Li, N.; Wang, F.; Hu, S. Atomic occupancy mechanism in brownmillerite Ca2FeAlO5 from a thermodynamic perspective. *J. Am. Ceram. Soc.* **2020**, *103*, 635–644. [CrossRef]
41. Jupe, A.C.; Cockroft, J.K.; Barnes, P.; Colston, S.L.; Sankar, G.; Hall, C. The site occupancy of Mg in the brownmillerite structure and its effect on hydration properties: An X-ray/neutron diffraction and EXAFS study. *J. Appl. Cryst.* **2001**, *34*, 55–61. [CrossRef]
42. De Clercq, H.; Jovanović, M.; Linnow, K.; Steiger, M. Performance of limestones laden with mixed salt solutions of Na_2SO_4–$NaNO_3$ and Na_2SO_4–K_2SO_4. *Environ. Earth Sci.* **2013**, *69*, 1751–1761. [CrossRef]
43. Rodriguez-Navarro, C.; Doehne, E. Salt weathering: Influence of evaporation rate, supersaturation and crystallization pattern. *Earth Surf. Process. Landf.* **1999**, *24*, 191–209. [CrossRef]
44. Linnow, K.; Steiger, M.; Lemster, C.; De Clercq, H.; Jovanović, M. In situ Raman observation of the crystallization in $NaNO_3$–Na_2SO_4–H_2O solution droplets. *Environ. Earth Sci.* **2013**, *69*, 1609–1620. [CrossRef]
45. Lindström, N.; Heitmann, N.; Linnow, K.; Steiger, M. Crystallization behavior of $NaNO_3$ -Na_2SO_4 salt mixtures in sandstone and comparison to single salt behavior. *Appl. Geochem.* **2015**, *63*, 116–132. [CrossRef]
46. Silcock, H.L. Solubilities of inorganic and organic compounds. In *Ternary and Multicomponent Systems of Inorganic Substances*; Pergamon Press: Oxford, UK, 1979; Volume 3.
47. Holtkamp, M.; Heijnen, W. The mineral darapskite in the efflorescence on two dutch churches. *Stud. Conserv.* **1991**, *36*, 175–178. [CrossRef]
48. Puşcaş, C.M.; Onac, B.P.; Tămas, T. The mineral assemblage of caves within Şălitrari Mountain (Cerna Valley, SW Romania): Depositional environment and speleogenetic implications. *Carbonates Evaporites* **2010**, *25*, 107–115. [CrossRef]
49. Domasłowski, W. *Preventive Conservation of Stone Historic Objects*; Wydawnictwo Uniwersytetu Mikołaja Kopernika: Toruń, Poland, 1993. (In Polish)
50. Doehne, E.; Price, C.A. *Stone Conservation: An Overview of Current Research*, 2nd ed.; Getty Conservation Institute: Los Angeles, CA, USA, 2010; p. 175.
51. Reports on the state of the environment in the Małopolska province (In Polish) 2010–2017. Wojewódzki Inspektorat Ochrony Środowiska w Krakowie: Kraków, Poland. Available online: http://www.krakow.pios.gov.pl (accessed on 10 December 2019).

52. Marszałek, M. Identification of secondary salts and their sources in deteriorated stone monuments using micro-Raman spectroscopy, SEM-EDS and XRD. *J. Raman Spectrosc.* **2016**, *47*, 1473–1485. [CrossRef]
53. Matuszko, D.; Piotrowicz, K.; Kowanetz, L. Components of the natural environment—Climate (in Polish with English summary). In *Natural Environment of Krakow. Resources—Protection—Management*, 2nd ed.; Baścik, M., Degórska, B., Eds.; Uniwersytet Jagielloński w Krakowie: Kraków, Poland, 2015; pp. 81–108.

© 2020 by the authors. Licensee MDPI, Basel, Switzerland. This article is an open access article distributed under the terms and conditions of the Creative Commons Attribution (CC BY) license (http://creativecommons.org/licenses/by/4.0/).